

## **Supplementary Materials for**

### **Lithosphere-asthenosphere interactions beneath Northeast**

### **China and the origin of its intraplate volcanism**

**Anqi Zhang<sup>1, 2, 3</sup>, Zhen Guo<sup>1, 3, \*</sup>, Juan Carlos Afonso<sup>2, \*</sup>, Heather Handley<sup>2</sup>,**

**Hongkun Dai<sup>2</sup>, Yingjie Yang<sup>2</sup>, Y. John Chen<sup>1, 3</sup>**

<sup>1</sup>Department of Ocean Science and Engineering, Southern University of Science and Technology,  
Shenzhen, 518055, China

<sup>2</sup>ARC Centre of Excellence for Core to Crust Fluid Systems (CCFS)/GEMOC, Department of Earth  
and Environmental Sciences, Macquarie University, North Ryde, NSW 2109, Australia

<sup>3</sup>Southern Marine Science and Engineering Guangdong Laboratory (Guangzhou), Guangzhou, 511458,  
China

**\*Corresponding authors**

E-mail address: [guoz3@sustc.edu.cn](mailto:guoz3@sustc.edu.cn); [juan.afonso@mq.edu.au](mailto:juan.afonso@mq.edu.au)

Submitted for consideration of publication in

*Geology*

June 2021

## 1. Methodology

### 1.1 Data

Geophysical data used in our multi-observable probabilistic inversion include fundamental mode Rayleigh wave dispersion data, absolute elevation, geoid height, and surface heat flow (SHF).

Rayleigh wave dispersion curves are taken from ambient noise tomography and teleseismic two-plane-wave tomography of a recent study by Fan et al. (2021), which generates Rayleigh wave phase velocity maps at 6-45 s periods and 45-143 s periods, respectively. The broadband dispersion curves that we use at 5-143 s are extracted from these two sets of dispersion maps by taking their averages at the overlapped period of 45 s (Fig. S1 a-c). More details about the data, tomography methods, and uncertainty estimation can be found in Fan et al. (2021). To take advantage of the original high resolution of the Rayleigh wave phase velocity maps, we subdivide our study region into 736 1D columns with a surface area of  $0.5^{\circ} \times 0.5^{\circ}$ .

Non-seismic data sets are collected from different sources: elevation data are taken from the GTOPO30 global elevation model (<http://lta.cr.usgs.gov/GEOPO30>, Fig. S1 f); filtered/upper mantle geoid height data are taken from Afonso et al. (2019) (Fig. S1 e) and SHF data come from the continental China heat flow data set of Jiang et al. (2019) (Fig. S1 d). A low-pass filter is used to remove the high-frequency components with the wavelengths  $< 50$  km in elevation. The filtered geoid minimizes/removes the effects of deep mantle ( $> 400$  km) anomalies that are not considered in the inversion. In their recent global study, Afonso et al. (2019) presented and scrutinized a filtered geoid model that explicitly accounted for whole-mantle anomalies. Based on their results, and considering the size of our study region, we conclude that the filtered geoid model of Afonso et al. (2019) is suitable for our purposes.

Some extreme SHF values ( $<20 \text{ mWm}^{-2}$  and  $>150 \text{ mWm}^{-2}$ ) are removed from the original dataset, which are believed to be associated with local, shallow perturbations from groundwater circulation. Based on the assumptions and limitations of the 1D approximation to solve the forward problems (Afonso et al., 2013a; 2013b; 2016a), we adopt a different resolution for the non-seismic data. Therefore, the elevation, geoid height and SHF data associated with each 1D column are computed using a moving average method with a window size of  $1^\circ \times 1^\circ$ . The means and variances computed for each  $1^\circ \times 1^\circ$  cell are used, respectively, as input data and associated uncertainty during the inversion. We assign minimum uncertainties to elevation and geoid height of 150 m and 1.2 m, respectively, to account for theoretical modeling errors (Afonso et al., 2013b). The standard deviation assigned to the SHF data is 20% of the mean SHF, with a minimum of  $10 \text{ mWm}^{-2}$  (Jaupart and Mareschal, 2011).

## **1.2 Thermochemical modelling**

The method used in this study has been particularly designed for constraining the present-day lithospheric thermal and compositional structure by incorporating data sets with different and complementary sensitivities to shallow/deep, thermal/compositional anomalies. Full descriptions of this method have been presented in detail in Afonso et al. (2013a; b; 2016a) and Qashqai et al. (2016; 2018). Therefore, we only provide a brief introduction to the main forward/inversion problems and model parameterization relevant to this study.

The forward problems involve: i) solving the steady-state heat transfer equation, ii) computing the stable mineral assemblages in the upper mantle and their physical properties (e.g.  $V_p$ ,  $V_s$ ,  $\rho$ ) via Gibbs free-energy minimization, iii) predicting geoid height and solving the isostatic balance equations (i.e., we assume that the present-day

elevations are isostatically supported, but the effects of dynamic topography are also tested and shown in Fig. S2), iv) calculating the fundamental mode Rayleigh wave dispersion curves and attenuation effects due to temperature-dependent anelasticity (cf. Afonso et al., 2013a; b; Qashqai et al., 2016). The inverse problem is solved by adopting a Bayesian inference approach. In this framework, prior information at hand on both observable data and model parameters are combined with information from observed data and physical models (i.e. forward problems). This allows us to derive a multidimensional probability density function (PDF) over the parameter and data space, known as the posterior PDF, which represents the most comprehensive solution to the inverse problem (Tarantola, 2005). We employ a Markov Chain Monte Carlo (MCMC) sampling method based on the Delayed Rejection Adaptive Metropolis (DRAM) algorithm of Haario et al. (2006) to sample the posterior PDF. In this study, we run 290,000 simulations per column and use 50,000 simulations in the initial pre-adaptive stage. Subsequently, we update the proposal distribution every 30,000 new samples (i.e. a total of eight adaptations). The total number of simulations for the entire region is 213.5 million (736 columns).

Each 1D column is parameterized into three crustal layers (upper/sediments, middle, and lower crust) and two upper mantle layers (lithospheric and sublithospheric mantle) (Fig. S3). Each crustal layer is characterized by its thermal conductivity ( $\kappa$ ), coefficient of thermal expansion ( $\alpha$ ), compressibility ( $\beta$ ), bulk density ( $\rho$ ),  $V_p/V_s$ , thickness ( $h$ ), and radiogenic heat production (RHP). Of these, the first three are assumed known (Table S1), while the others are inverted for. Priors for these unknown crustal parameters are given in Table S2. The initial sedimentary thickness is taken from the CRUST1.0 model (Laske et al., 2013) and the depth to the Moho is taken from the receiver function study of Li et al. (2014). The bulk compositions of the lithospheric



and sublithospheric mantle are defined by five major oxides within the system CaO-FeO-MgO-Al<sub>2</sub>O<sub>3</sub>-SiO<sub>2</sub> (priors are also listed in Table S2).

The temperature distribution inside the lithosphere is obtained by solving the steady-state heat transfer equation subject to Dirichlet boundary conditions at the surface (typically  $T_s=10$  °C) and at the bottom of the lithosphere ( $T_{LAB}=1250$  °C) within a finite-difference mesh (red dots in Fig. S3). In the sublithospheric mantle (i.e. convection-dominated layer), temperature is a free parameter retrieved by linear interpolation between “temperature nodes” located at different depths (base of the transition layer  $T_{Buffer}$ , three intermediate nodes  $T_{inter1}$ ,  $T_{inter2}$ ,  $T_{inter3}$  and bottom of the model  $T_{bottom}$ ). These five unknown parameters are sampled by the DRAM algorithm during the MCMC inversion and their priors are listed in Table S2. Then the equilibrium assemblages and their thermophysical properties (e.g.  $V_p$ ,  $V_s$ ,  $\rho$ , etc.) are computed at each “thermodynamic node” (blue squares in Fig. S3) via Gibbs free-energy minimization using components of the Perple\_X software (Connolly, 2009) and the thermodynamic database of Xu et al. (2008). All these computed velocities and densities are linearly interpolated to the fine mesh during the forward calculations of dispersion curves. The data fits of this inversion are shown in Fig. S4.

### 1.3 Melting model

We estimate melt fractions in the mantle based on the inverted temperature ( $T$ ), the solidus temperature ( $T_S$ ) and the liquidus temperature ( $T_L$ ) as follows (Katz et al., 2003):

$$F_{melt} = \left(\frac{T-T_S}{T_L-T_S}\right)^{1.5}. \quad (1)$$

where  $F_{melt}$  represents melt fraction, and  $T_S$  and  $T_L$  are computed as:

$$T_S = 1085.7 + 132.9P - 5.1P^2 \quad (2)$$

$$T_L = 1780 + 45P - 2P^2 \quad (3)$$

where  $P$  is pressure in GPa. Two significant simplifying assumptions are that both the solidus and liquidus temperatures used here are representative of dry peridotite only and no melting history or latent heat effects are considered. Thus, predicted melt fractions should be taken with caution and as first order estimates only. The effect of melt on seismic velocities is also considered based on the results of Clark and Lesher (2017), assuming a maximum melt fraction retention in the mantle of 5% (any melt predicted above this threshold is assumed to be completely extracted from the mantle and therefore it cannot affect seismic velocities). The reductions in compressional wave ( $\Delta V_P$ ) and shear wave ( $\Delta V_S$ ) velocities as functions of melt fraction are:

$$\Delta V_P = \left[ \frac{\frac{(\beta-1)\Lambda_K + \frac{4}{3}\gamma\Lambda_G}{1 + \frac{4}{3}\gamma} - \left(1 - \frac{\rho_L}{\rho_S}\right) \right] \frac{F_{melt}}{2} \quad (4)$$

$$\Delta V_S = \left[ \Lambda_G - \left(1 - \frac{\rho_L}{\rho_S}\right) \right] \frac{F_{melt}}{2} \quad (5)$$

where  $\beta$  is the ratio of the adiabatic bulk moduli of the solid to that of the liquid,  $\gamma$  is the ratio of the shear modulus to adiabatic bulk moduli for the solid phases,  $\rho_L$  and  $\rho_S$  are densities of the silicate melt and crystalline mantle, respectively, and  $\Lambda_K$  and  $\Lambda_G$  are geometric factors of pore shape. Approximate values of these parameters can be found in Clark and Lesher (2017) and Takei (2002), thus  $\Delta V_P$  and  $\Delta V_S$  can be estimated by  $\Delta V_P = -1.9F_{melt}$  and  $\Delta V_S = -2.4F_{melt}$ , respectively. These two equations establish near-linear relations between the reductions in velocities and melt fraction in mantle depth at relatively low melt fraction ( $\leq 10\%$ , Clark and Lesher, 2017). Therefore, the seismic velocities ( $V_P$  and  $V_S$ ) after considering the effect of the melt can be calculated by:

$$V_P = V_{P\_sys} - 1.9 * F_{melt} * V_{P\_sys} \quad (6)$$

$$V_S = V_{S\_sys} - 2.4 * F_{melt} * V_{S\_sys} \quad (7)$$

where  $V_{P\_sys}$  and  $V_{S\_sys}$  are the seismic velocities of a system without melting (but

including attenuation effects due to temperature-dependent anelasticity). It is worth noting that although the presence of melt will also reduce the bulk density, we neglect this effect since it is always small compared to the uncertainties in data sets constraining the bulk density (Afonso et al., 2016).

## **2. Mafic melts may have been trapped beneath central-east SLB**

We note that a thermal anomaly and thin lithosphere (Fig. 2a, Fig. S7a) is imaged beneath the central-east SLB, where our model also predicts partial melting in the mantle (Fig. 2b). Yet, there is no evidence of recent magmatism on the surface in this region. Given the thick sedimentary sequence in this part of the basin, mafic melts generated in the sublithospheric mantle may have been preferentially emplaced at deeper levels in the crust and/or as sills within the sedimentary units. Indeed, this hypothesis is supported by the high  $V_p/V_s$  values (i.e. presence of mafic rocks) that we image in this region at mid-low crustal depths (Fig S7c, d); similar  $V_p/V_s$  values have been reported in Tao et al. (2014). There is also independent evidence for mafic crustal components beneath the SLB based on the high shear wave velocity imaged at mid-lower crustal depths (Guo et al., 2015). Alternatively, the shallow asthenospheric mantle beneath this region could be more refractory than what we assumed to estimate melt fractions (e.g. as a result of previous melting episodes) and therefore less prone to generating melts.

To verify the reliability of our predicted mantle temperatures and melt content beneath the SBL, and to assess any potential influence that the thick low-velocity sediments may have on the deep structure, we conducted a number of tests. We first construct four synthetic models and compute their associated Rayleigh wave dispersion curves (see Figure S8): i) a model without sediments and with mantle temperatures

below the solidus (blue line); ii) a model without sediments and with mantle temperatures above the solidus at  $\sim 80$  km depth (purple line); iii) a model with a 4 km thick sedimentary layer (shear wave velocity  $\sim 2.3$  km/s) and mantle temperatures below the solidus (red line); and iv) a model with a 4 km thick sedimentary layer and mantle temperatures above the solidus at  $\sim 80$  km depth (cyan line). As expected, these models demonstrate that sediments influence the dispersion curves mainly at low periods ( $< 40$  s), while the deep mantle temperature influences dispersion curves at long periods ( $> 30$  s). Although there is some influence from sediments on periods longer than 40 s, they are well within uncertainties.

We also run four inversions using these synthetic dispersion curves. Fig. S8b shows the inverted temperature structures as the mean of the posterior probability density function. The inverted temperatures (red line) using the synthetic dispersion curve from model (iii) does not show a higher temperature than the solidus. Therefore, we conclude that it is unlikely that the low-velocity basin (with a sediment thickness of  $\sim 4$  km) would influence the inversion (and/or dispersion curves) in a way that artificially high temperatures (and associated melts) would be obtained in the mantle. Consequently, the predicted high-temperatures and associated partial melting beneath the central-east SLB seem to be a robust feature.

### **3. Evaluation of contamination and source variations**

Although samples with  $\text{MgO} > 6\%$  should not have been significantly affected by fractionation or contamination, we cannot completely rule out these and other effects (e.g. a pyroxenitic component in the source) on the composition of the basalts. However, there are several lines of evidence that suggest that contamination and/or source heterogeneity cannot be the main factor controlling the composition of the basalts. First,

the common occurrence of mantle xenoliths in erupted volcanic rocks throughout the region suggests that magma ascended rapidly, with limited interaction with the crustal materials (Zhang and Guo, 2016; Wang et al., 2017; Yu et al., 2018). Second, the Sr-Nd-Pb isotope composition of basalts with ages  $< 5$  Ma show no correlation with eruption age and/or location (Fig. S11). Third, the observed correlations between both the foci of volcanism and its average composition with lithospheric thickness and sublithospheric temperature anomalies (Figs. 2, 3 and S10) are unlikely to be coincidental. If source composition was the main factor controlling the compositional variability of the basalts, we should not see these correlations unless the composition of the source was also correlated with both lithospheric thickness and sublithospheric temperature anomalies. In summary, the evidence above indicate that a dominant effect from variations in mantle source composition is unlikely.

## References not presented in main text

- Afonso, J. C., Salajegheh, F., Szwillus, W., Ebbing, J., and Gaina, C. (2019). A global reference model of the lithosphere and upper mantle from joint inversion and analysis of multiple data sets. *Geophysical Journal International*, **217**, 1602-1628, doi: 10.1093/gji/ggz094.
- Connolly, J. A. D. (2009). The geodynamic equation of state: what and how. *Geochemistry Geophysics Geosystems*, 10(10), Q10014, doi: 10.1029/2009GC002540.
- Davies, D. R., Valentine, A. P., Kramer, S. C., Rawlinson, N., Hoggard, M. J., Eakin, C. M., and Wilson, C. R. (2019). Earth's multi-scale topographic response to global mantle flow. *Nature Geoscience*, **12**, 845-850, doi: 10.1038/s41561-019-0441-4.
- Deng, Y. F., and Levandowski, W. (2018). Lithospheric alteration, intraplate crustal deformation, and topography in eastern China. *Tectonics*, **37**, 4120-4134, doi: 10.1029/2018TC005079.
- Fan, X. L., Chen, Q. F., Ai, Y. S., Chen, L., Jiang, M. M., Wu, Q. J., and Guo, Z. (2021). Quaternary sodic and potassic intraplate volcanism in northeast China controlled by the underlying heterogeneous lithospheric structures. *Geology*.
- Guo, Z., Chen, Y. J., Ning, J. Y., Feng, Y. G., Grand, S. P., Niu, F. L., Kawakatsu, H., Tanaka, S., Obayashi, M., and Ni, J. (2015). High resolution 3-D crustal structure beneath NE China from joint inversion of ambient noise and receiver functions using NECESSArray data. *Earth and Planetary Science Letters*, **416**, 1-11, doi: 10.1016/j.epsl.2015.01.044.
- Haario, H., Laine, M., Mira, A., and Saksman, E. (2006). DRAM: Efficient adaptive MCMC. *Statistics and Computing*, **16**(4), 339-354, doi: 10.1007/s11222-006-9438-0.
- Jaupart, C. and Mareschal, J. C. (2011). Heat Generation and Transport in the Earth, Cambridge University Press, Cambridge.
- Jiang, G. Z., Hu, S. B., Shi, Y. Z., Zhang, C., Wang, Z. T., and Hu, D. (2019). Terrestrial heat flow of continental China: Updated dataset and tectonic implications. *Tectonophysics*, **753**, 36-48, doi: 10.1016/j.tecto.2019.01.006.
- Laske, G., Master, G., Ma, Z., and Pasyanos, M. (2013). Update on CRUST1.0 - A 1-Degree Global Model of Earth's CRUST, EGU Ge.
- Li, Y. H., Gao, M. T., and Wu, Q. J. (2014). Crustal thickness map of the Chinese mainland from teleseismic receiver functions. *Tectonophysics*, **611**, 51-60, doi: 10.1016/j.tecto.2013.11.019.
- Qashqai, M. J., Afonso, J. C., and Yang, Y. J. (2016). The crustal structure of the Arizona Transition

- Zone and southern Colorado Plateau from multiobservable probabilistic inversion, *Geochemistry Geophysics Geosystems*, **17**, 4308–4332, doi: 10.1002/2016GC006463.
- Qashqai, M. J., Afonso, J. C., and Yang, Y. J. (2018). Physical state and structure of the crust beneath the Western-Central United States form multi-observable probabilistic inversion. *Tectonics*, **37**, 3117-3147, doi: 10.1029/2017TC004914.
- Smith, W. H. F., and Wessel, P. (1990). Gridding with continuous curvature splines in tension. *Geophysics*, **55**(3), 293-305, doi: 10.1190/1.1442837.
- Takei, Y. (2002). Effect of pore geometry on VP/VS: from equilibrium geometry to crack. *Journal of Geophysical Research*, **107**, B2, 2043, doi: 10.1029/2001JB000522.
- Tao, K., Niu, F. L., Ning, J. Y., Chen, Y. J., Grand, S., Kawakatsu, H., Tanaka, S., Obayashi, M., and Ni, J. (2014). Crustal structure beneath NE China imaged by NECESSArray receiver function data. *Earth and Planetary Science Letters*, **398**, 48-57, doi: 10.1016/j.epsl.2014.04.043.
- Tarantola, A. (2005). Inverse problem theory and methods for model parameter estimation. Philadelphia, PA: Society for Industrial and Applied Mathematics.
- Xu, W., Lithgow-Bertelloni, C., Stixrude, L., and Ritsema, J. (2008). The effect of bulk composition and temperature on mantle seismic structure. *Earth and Planetary Science Letters*, **275**, 70-79, doi: 10.1016/j.epsl.2008.08.012.
- Zhang, M. L., and Guo, Z. F. (2016), Origin of Late Cenozoic Abaga–Dalinuoer basalts, eastern China: Implications for a mixed pyroxenite–peridotite source related with deep subduction of the Pacific slab. *Gondwana Research*, **37**, 130-151, doi: 10.1016/j.gr.2016.05.014.

Fig. S1. Geophysical data used in the multi-observable probabilistic inversion. Examples of Rayleigh wave phase velocity maps from (a) ambient noise tomography (ANT), (c) two-plane-wave tomography (TPWT) and (b) the combined ANT + TPWT dataset for three different periods; (d) Surface heat flow; (e) Geoid height; (f) Topography. Gray triangles in c) are the seismic stations. Colored dots in d) indicate the available measurements in NEC which are interpolated onto the whole study area with a gridding method based on continuous curvature splines (Smith and Wessel, 1990). Given the poor coverage of this dataset, we assign large uncertainties to it (see Methods).

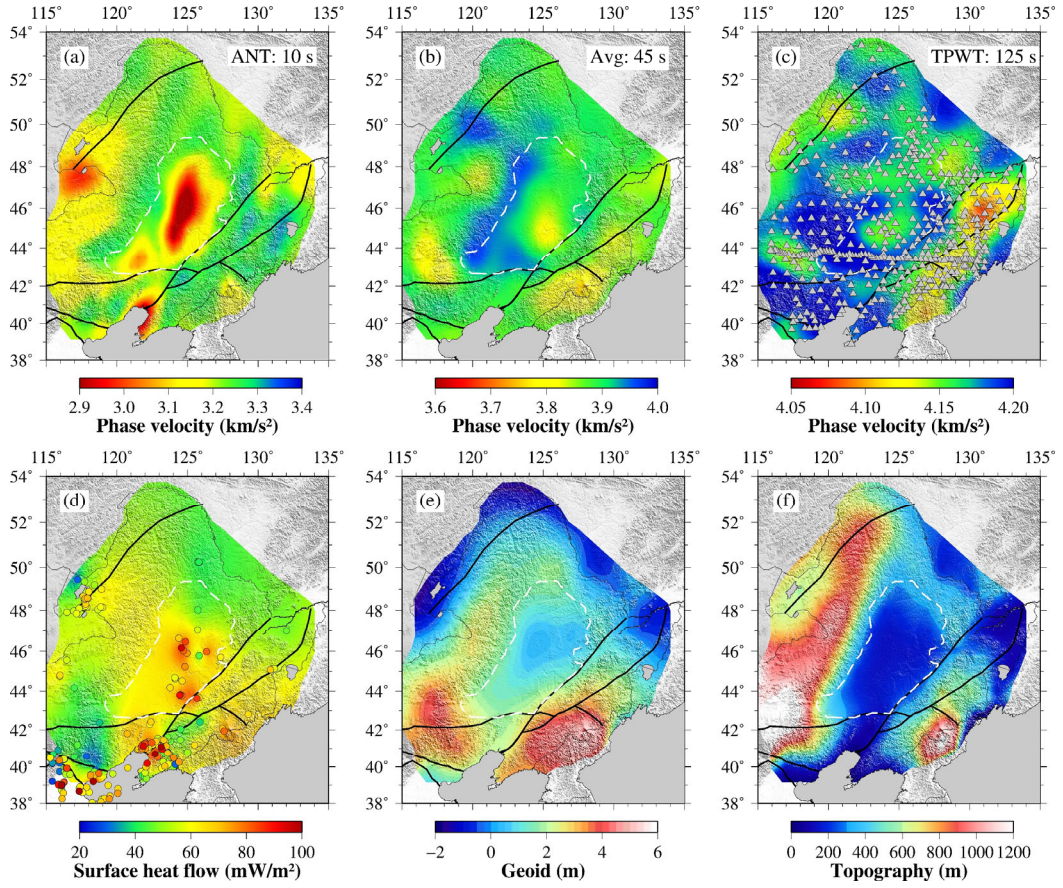




Fig. S2. Potential effects of dynamic topography on inversion results. The first row shows the observed input topography (a) and the inverted Moho (b) and LAB (c) depths discussed in the main text. The second row shows the results for Moho (e) and LAB (f) depths when the input topography contains a positive dynamic contribution of 400 m (panel d; Davies et al., 2019). The third row shows the same results as in (d-f) but for an input topography that contains a dynamic contribution of -400 m. Note that the inversion results are robust against expected dynamic contributions and they overlap at the level of 1 standard deviation (Figs. S5 and S7b).

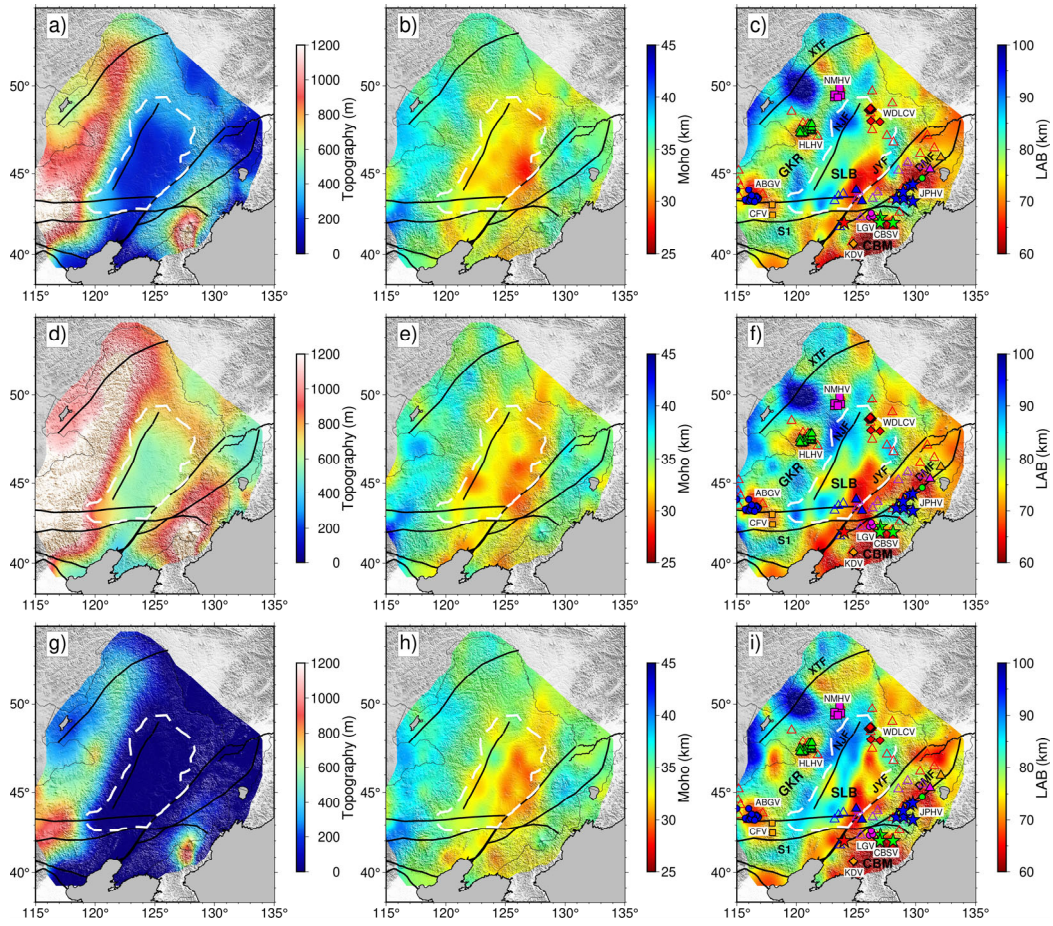


Fig. S3. Model parameterization used in the 1D inversion of each  $1^\circ \times 1^\circ$  cell, modified from Afonso et al. (2013) and Zhang et al. (2019). Blue points along the geotherm (intermediate nodes) represent the points where full Gibbs free-energy minimization is performed during the MCMC inversion.

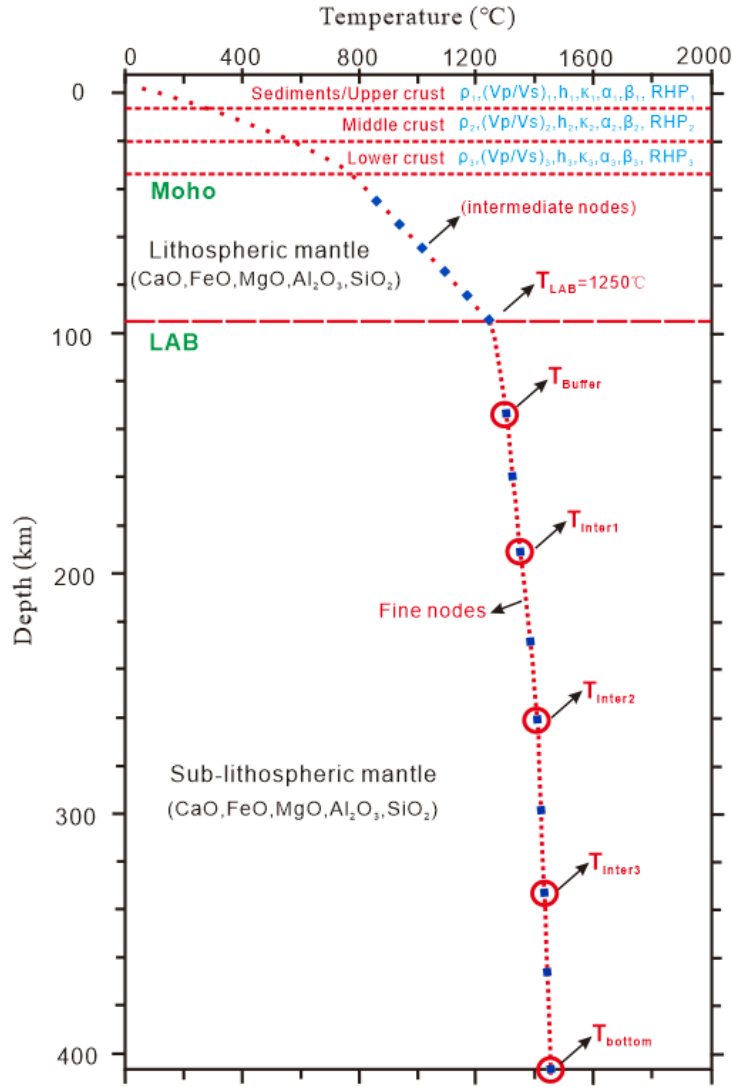


Fig. S4. Left column: predicted data from the inversion (Rayleigh wave phase velocity maps for periods of 10 s, 45 s, and 125 s; SHF, geoid height, and topography). Second column: absolute differences between the means of the observed and predicted observables. The right two columns are the data fits for three representative locations in GXR, SLB, and CBM. The data fit for SHF is generally poorer than for other datasets. This is mostly because of the larger uncertainties assigned to this observable. Despite this, the predicted SHF is still within the assumed uncertainties.

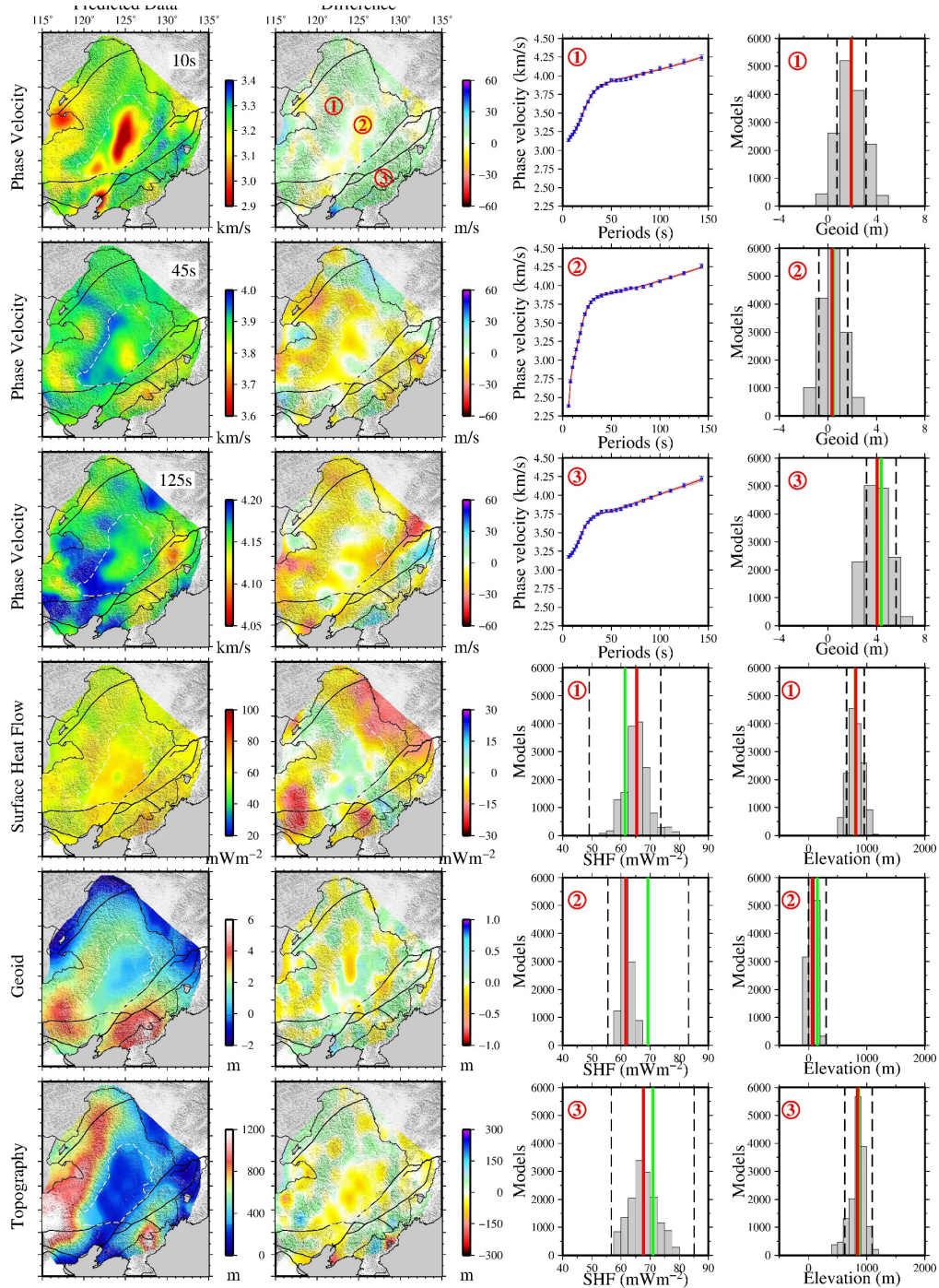




Fig. S5. Map of uncertainty (as  $1\sigma$  of the posterior PDF) of LAB depth.

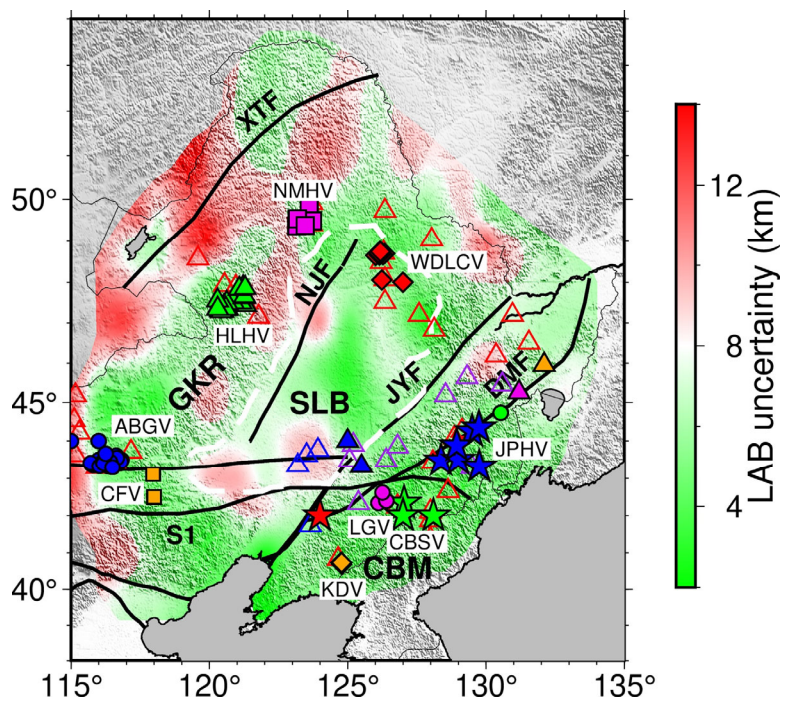


Fig. S6. (a) Depths at which partial melting in the mantle is predicted. (b) A temperature profile crosses the KDV, CBSV, and JPHV; the Moho and LAB depths are indicated with white and purple solid lines, respectively. Although there is more melt predicted under the region between the CBSV and JPHV (Fig. 2 in main text), the melt is generated at deeper levels and under a thicker lithosphere than in the surrounding regions that contain recent volcanism. Shallower melts may be extracted to the surface more efficiently under thinned regions than deeper melts under thick lithospheres.

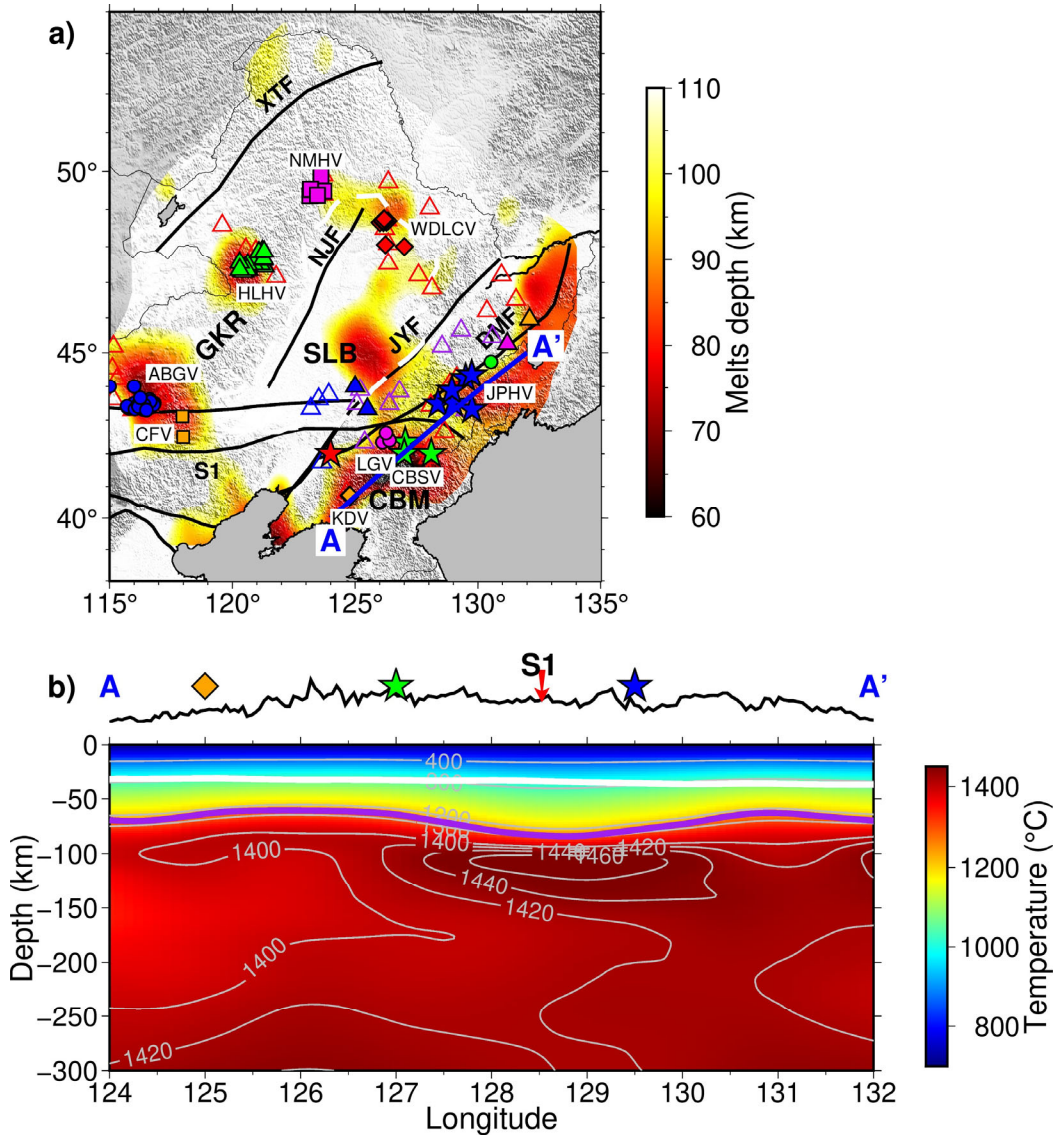


Fig. S7. a) Moho depth, b) associated uncertainty as  $1\sigma$  of the posterior PDF, c)  $V_p/V_s$  of the middle crust and d)  $V_p/V_s$  of the lower crust.

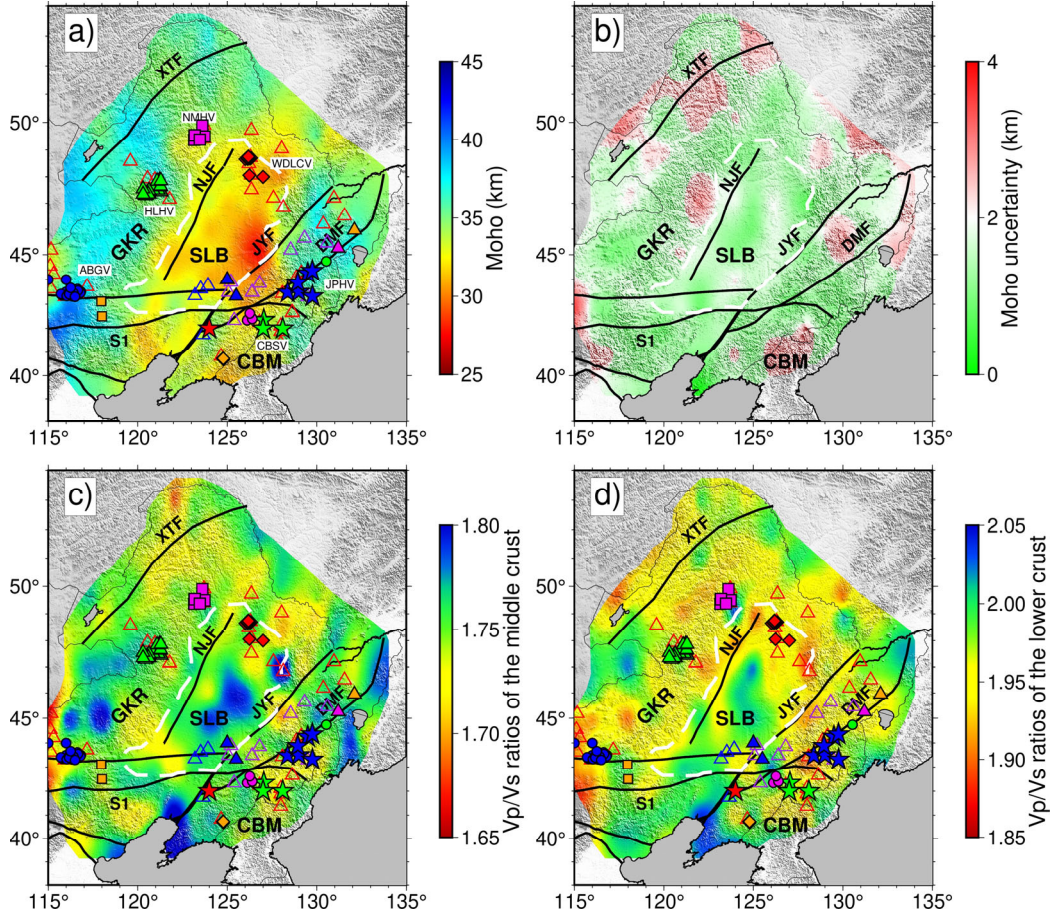


Fig. S8. a) Predicted Rayleigh wave dispersion curves based on the four synthetic models explained in the text. b) Corresponding inverted geotherms (as the mean of the posterior probability density function); note that the cyan line is covered by the purple line.

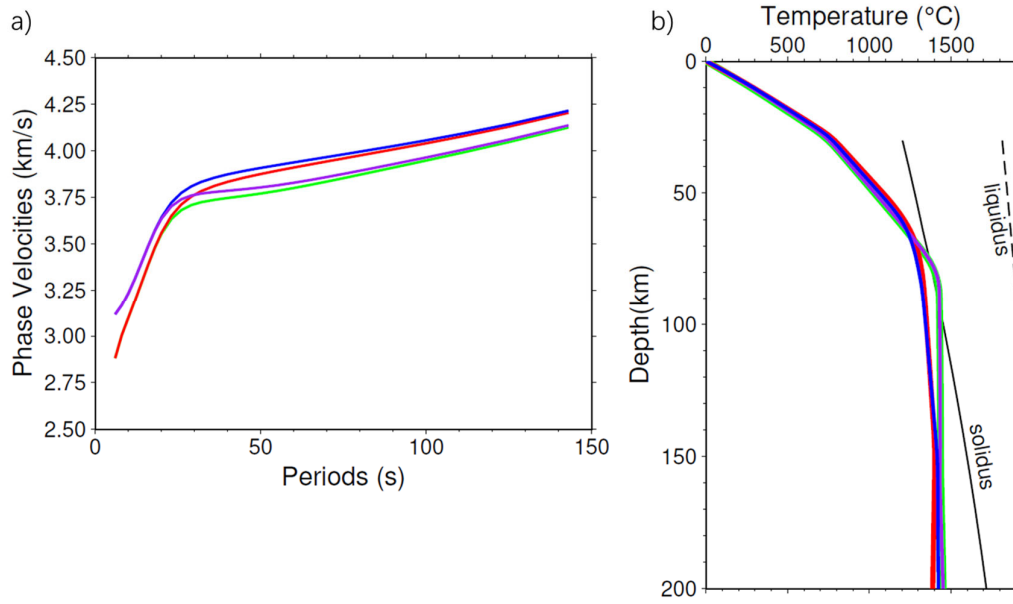


Fig. S9. Systematic variations in ratios of more- to less-incompatible elements as a function of LAB depth. Grey arrows highlight the general trend between lithospheric thickness and geochemical proxies of degree of melting.

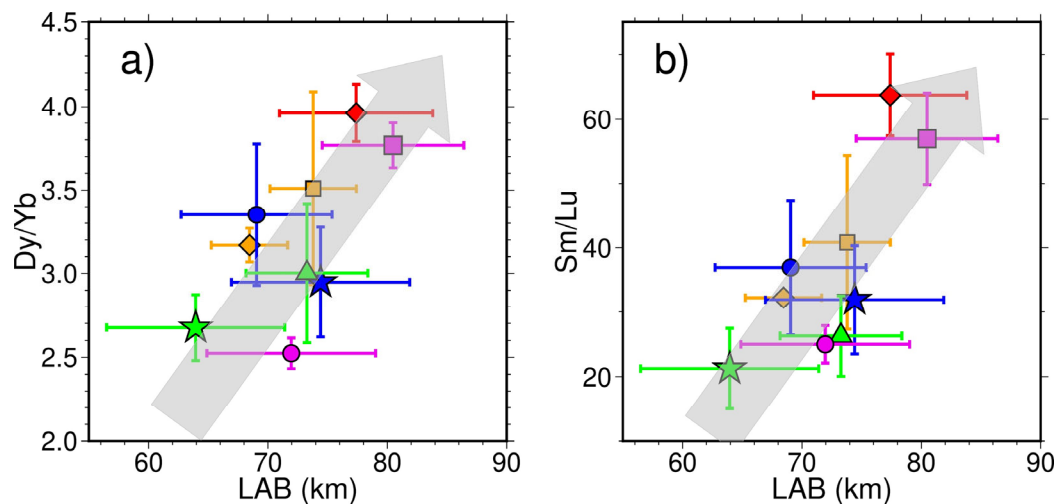


Fig. S10. Systematic variations in ratios of more- to less-incompatible elements as a function of melt fraction. Grey arrows highlight the general trend between melt fraction and geochemical proxies of degree of melting.

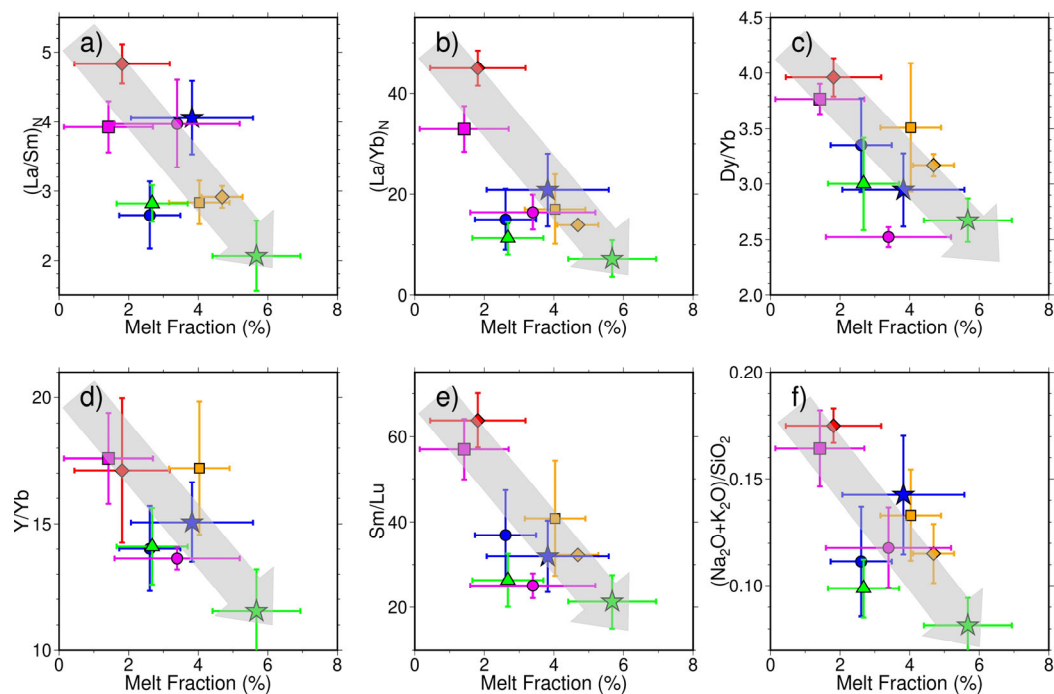




Fig. S11. Sr-Nd-Pb isotope composition of the young basalts in NEC correlate neither with the eruption age nor with the relative distance from a common point (130° E, 40° N).

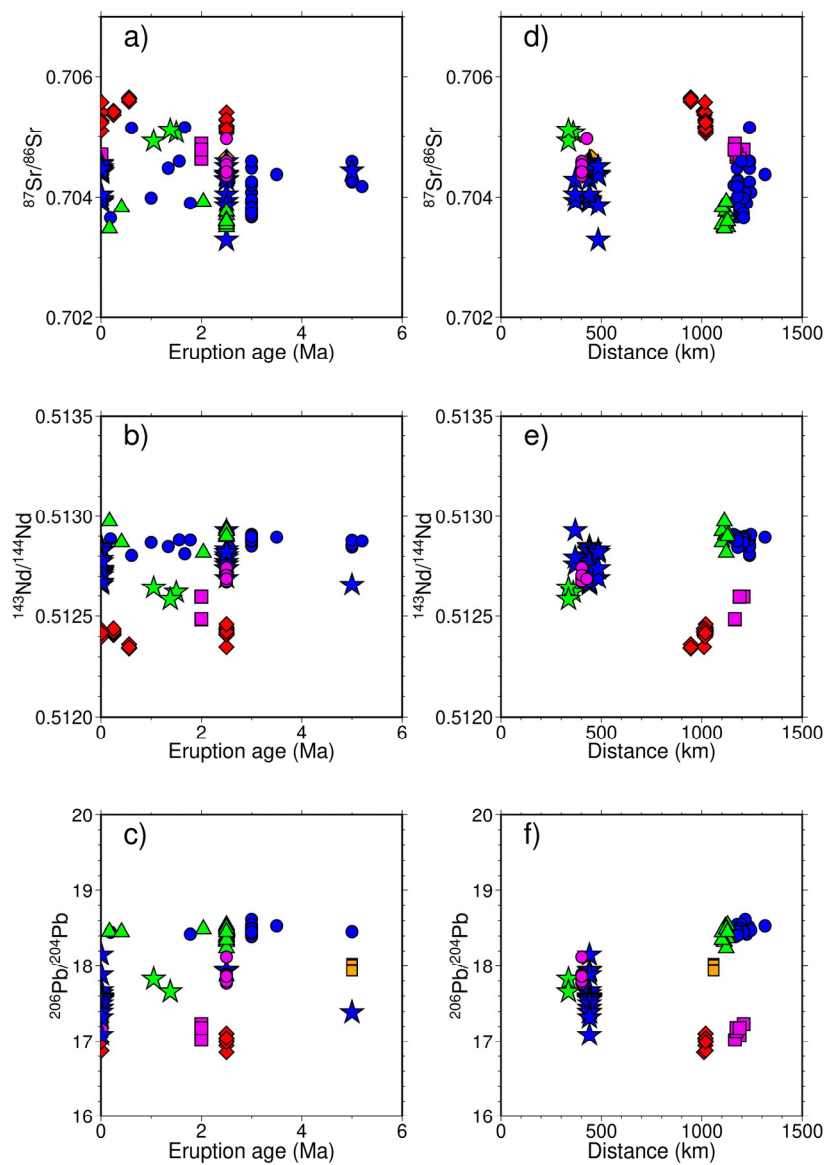


Table S1. Constant crustal parameters.

Parameter	Value
$\kappa_1 (Wm^{-1}\text{°C}^{-1})$	2.4
$\kappa_2 (Wm^{-1}\text{°C}^{-1})$	2.3
$\kappa_3 (Wm^{-1}\text{°C}^{-1})$	2.1
$\alpha_1 (\text{°C}^{-1})$	$2.7 \times 10^{-5}$
$\alpha_2 (\text{°C}^{-1})$	$2.6 \times 10^{-5}$
$\alpha_3 (\text{°C}^{-1})$	$2.3 \times 10^{-5}$
$\beta_1 (Pa^{-1})$	$5.0 \times 10^{-11}$
$\beta_2 (Pa^{-1})$	$1.4 \times 10^{-11}$
$\beta_3 (Pa^{-1})$	$1.1 \times 10^{-11}$

Subscripts 1, 2 and 3 denote the three crustal layers.  $\kappa$ : thermal conductivity;  $\alpha$ : coefficient of thermal expansion;  $\beta$ : compressibility.

Table S2. Unknown parameters and their initial prior ranges.

Parameter	Range
Crust	
Density (first crustal layer) (kg/m <sup>3</sup> )	2000-2500
Density (second crustal layer) (kg/m <sup>3</sup> )	2600-3000
Density (third crustal layer) (kg/m <sup>3</sup> )	2800-3200
$V_P/V_S$ (first crustal layer)	1.85-2.05
$V_P/V_S$ (second crustal layer)	1.65-1.85
$V_P/V_S$ (third crustal layer)	1.85-2.10
$\Delta h$ (first crustal layer) (km)	-2.0-2.0
$\Delta h$ (second crustal layer) (km)	-5.0-5.0
$\Delta h$ (third crustal layer) (km)	-5.0-5.0
RHP ( $\mu\text{W}/\text{m}^3$ )	0.4-1.8
Mantle	
LAB (km)	50-200
Al <sub>2</sub> O <sub>3</sub> in the lithosphere (wt.%)	0.5-5.5
FeO in the lithosphere (wt.%)	6.0-9.2
MgO in the lithosphere (wt.%)	34.0-55.0
CaO in the lithosphere (wt.%)	0.2-5.2
Al <sub>2</sub> O <sub>3</sub> in the sublithosphere (wt.%)	0.5-5.5
FeO in the sublithosphere (wt.%)	6.0-9.2
MgO in the sublithosphere (wt.%)	34.0-55.0
CaO in the sublithosphere (wt.%)	0.2-5.2
Tbuffer (°C)	1230-1550
Tint1 (°C)	1250-1560
Tint2 (°C)	1300-1580
Tint3 (°C)	1330-1580
Tbottom (°C)	1430-1650